Towards more realistic simulations of microstructural evolution in oxidic systems

Inge Bellemans[1*], Nico Vervliet[2], Lieven De Lathauwer[2,3], Nele Moelans[4], Kim Verbeken[1]

[1] *Department of Materials, Textiles and Chemical Engineering, Ghent University, Tech Lane Ghent Science Park - Campus A, Technologiepark Zwijnaarde 46, 9052 Gent, Belgium*

[2] *Department of Electrical Engineering (ESAT), KU Leuven, Kasteelpark Arenberg 10 (box 2446), 3001 Leuven, Belgium*

[3] *Group Science, Engineering and Technology, KU Leuven - Kulak, E. Sabbelaan 53, 8500 Kortrijk, Belgium*

[4] *Department of Materials Engineering, KU Leuven, Kasteelpark Arenberg 44 (box 2450), 3001 Leuven, Belgium*

KEYWORDS

Phase field model, Thermodynamic database coupling, Canonical polyadic decomposition, Crystal growth, Magnetite

ABSTRACT

High temperature oxidic systems are encountered in nature (magma chambers) and pyrometallurgical processes. In these systems, the solidification of the oxidic liquids influences the flow, the cooling after tapping, the viscosity and rheological behaviour within the reactor and also the freeze lining behaviour. On the mesoscale, the phase field concept has proved to be a very powerful tool for modeling crystallizing microstructures. However, application of the method to slag solidification is still challenging. In this work, we present a phase field model to simulate the faceted crystallization of Fe_3O_4 in a quaternary FeO-Fe_2O_3-Cu_2O-SiO_2 melt under different partial pressures of oxygen to solve certain problems encountered related to more realistic simulations in oxidic systems. The ratio of FeO/Fe_2O_3 at the upper boundary is in equilibrium with the oxygen fugacity of the atmosphere, while conserving Fe. Two-dimensional simulations are performed with different varying oxygen fugacity in the atmosphere. For the considered composition range, the growth velocities of the spinel crystals increase with decreasing oxygen fugacity. One of the focus points in creating more realistic phase field models is the incorporation of the thermodynamic driving forces in multicomponent multiphase-field models by coupling to thermodynamic databases. The first part of this work used a tabular method. However, as the number of components in the system increases, the number of thermodynamic data points also increases exponentially, and so do the computational and memory requirements. A possible solution for this might be the use of a canonical polyadic decomposition of the tensors containing the thermodynamic data. In this way, the huge tensors are approximated well by compact multilinear models or decompositions. This promising solution has been applied in the second part of this work on the same oxidic liquid-solid system.

[*] Corresponding author: Inge.Bellemans@UGent.be; Kim.Verbeken@UGent.be

1 INTRODUCTION

Crystallization of silicate melts takes place in geology [1], pyrometallurgy and glass making. In pyrometallurgy, the solidification of slags influences the slag cooling after tapping [2], the decantation behaviour [3], the viscosity and rheological behaviour within the reactor [4,5] as well as the freeze lining behaviour [6]. Modeling of silicate melt crystallization is frequently done on the macroscopic level, using thermodynamic equilibrium calculations to determine the fractions of all phases as a function of temperature. The Factsage software and database package [7] already proved its usefulness in pyrometallurgical applications, for example to model the phase mixture after solidification of a stainless steel slag [2].

Crystallization of phases typically results in complex morphologies on the mesoscale, e.g. dendrites or faceted growth. On this mesoscale, the phase field concept has proved to be a very powerful tool [8,9] for modeling crystallizing microstructures, because it can treat arbitrarily complex interface shapes with minimal mathematical complexity. In contrast to macroscopic models, the diffusion profiles and crystallization kinetics can be described as well as the morphology of individual crystals. First, Kobayashi [10] simulated a growing dendrite in a pure undercooled metallic liquid.

A number of phase-field model types have been proposed for binary alloy systems and may be divided into groups depending on the construction of the local free-energy functions. [11] The first type is a model by Wheeler, Boettinger, and McFadden (WBM) [12]. In this type of model, points within the interfacial region are assumed to be a mixture of solid and liquid both with the same composition. Consequently, problems can arise when upscaling the diffuse interface width for computational efficiency. [13,14] The second type is a model by Steinbach et al. [15] which assumes the interfacial region to be a mixture of solid and liquid with different compositions, fixed by a quasi-equilibrium condition. This multiphase system framework was further extended by Tiaden et al. [16] to a framework with coupled diffusion and phase field equations in multicomponent systems. Kim et al. [17] showed later that the quasi-equilibrium condition is equivalent to the equality of the phase diffusion potentials for locally coexisting phases and developed a more general version of this type of phase-field model, usually abbreviated as the KKS model.

The phase field method was mostly applied for metallic systems previously, until Heulens et al. [19] developed a multicomponent phase field model for the crystallization in slags, which was based on the KKS model. However, application of the method to slag solidification remains challenging. This work aimed at solving certain problems encountered related to more realistic simulations in oxidic systems. First, the peculiarities of oxidic systems have been investigated: the anisotropy, the influence of oxygen fugacity and then the thermodynamic data coupling for quaternary systems.

For oxide systems, the thermodynamic functions and diffusion data are expressed as a function of oxide components and not as a function of the elements. The model can be coupled with a thermodynamic database for oxides (FTOxid, from Factsage via Chemapp) to obtain the bulk thermodynamic properties of the liquid slag as a function of composition. The slag is described

in this database with the Modified Quasi-Chemical Model. Similar as previously described by Hu et al. [20], the model of Heulens et al. [19] modelled the stoichiometric solid phases with a paraboloid Gibbs energy with specific constraints to ensure correct phase equilibria and minimal solubility in the stoichiometric phase. The model was able to describe both crystallization and dissolution of the stoichiometric phase. The interfacial mobility and interfacial energy were modelled with anisotropy, as both faceted and dendritic crystallization can take place in oxide systems. Anisotropic interfacial energies are encountered frequently, as illustrated by [19,21–26] and the references therein. The anisotropy in interfacial energy was described similarly as by Kobayashi [10]. However, for growing spinel crystals, such as Fe_3O_4, crystallizing in a silicate melt, it is often accepted that the faceted growth is a consequence of a strong anisotropy in the solid–liquid interface kinetics. This is in contrast with most of the previous work considering anisotropy in surface energy. This kinetic anisotropy was introduced by Heulens et al. [19] and was based on the work of Uehara and Sekerka [27]. This will be investigated for a multicomponent system in the current work, focussing on the growth of the solids.

The local oxidation state of multivalent ions in slags, such as iron (i.e. ferrous (Fe^{2+}) and ferric (Fe^{3+}) cations) is important for the slag properties, such as the potential of the slag to oxidize. If an iron-bearing silicate melt is not in thermodynamic equilibrium with its oxygen-containing atmosphere, the melt is subjected to a redox reaction. The ratio of FeO/Fe_2O_3 at the upper boundary is in equilibrium with the oxygen fugacity of the atmosphere, while conserving Fe. Two-dimensional simulations can be performed with different varying oxygen fugacity in the atmosphere. In this model, the diffusion is assumed to be much slower than the redox reaction kinetics, and the redox ratio of FeO/Fe_2O_3 is thus locally in equilibrium with the oxygen activity in the melt. [19]

The biggest drawback of the model of Heulens et al. [19]was its limitation to only three oxidic components. In this work, the implementation of the model is adapted to extend the applicability to actual multicomponent systems, which is more relevant for realistic metallurgical oxidic systems. This was done in two different ways. First, through a similar coupling to the thermodynamic database as proposed by Heulens [19], but considering more elements, which happened through a tabulation method. The influence of the anisotropy and the partial pressure of oxygen on the faceted spinel growth was investigated in this way. The constructed model is used to simulate faceted growth of Fe_3O_4 in a $FeO\text{-}Fe_2O_3\text{-}Cu_2O\text{-}SiO_2$ system assuming different partial pressures of oxygen in the atmosphere above the melt.

However, we experienced that the coupling to a thermodynamic database becomes increasingly intricate as the number of components in the system increases. The exponential dependency of the amount of data on the number of components is called the curse of dimensionality [28]. To solve this problem, alternatives were also investigated in this work for the storage and handling of the thermodynamic data required for the phase field simulations. A possible solution was found in a canonical polyadic decomposition of the tensors containing the thermodynamic data. This method was already applied to metallic systems [29] before, but it is, in this work, applied for the first time to oxidic systems. With this method, the huge tensors are approximated well

by compact multilinear models or decompositions. In this work, a fourth-order canonical polyadic decomposition (CPD) of the original tensors is implemented in the phase field code.

2 MODEL AND IMPLEMENTATION

2.1 FREE ENERGY FUNCTIONAL

The total free energy of a heterogeneous isothermal system with *p* phases and *c* components is formulated as a functional of the non-conserved phase field variables η_i and the conserved concentration fields x_k (i.e. the mole fractions of the different components). The current work considered two phases, i.e. solid precipitate and liquid slag, even though the model can describe multiple solid precipitates growing or dissolving in the liquid. The presence of multiple solids was investigated by Heulens et al. [30].

The free energy functional decreases monotonously during microstructural evolution towards thermodynamic equilibrium and consists of interfacial and bulk Gibbs free energies, but no elastic or magnetic contributions were considered:

$$F = \int f(\eta_i, \vec{\nabla}\eta_i, x_k)\, dV = \int [f_¿(\eta_i, \vec{\nabla}\eta_i) + f_b(\eta_i, x_k)]\, dV \quad (1)$$

In this model, the interfacial free energy density is represented by:

$$f_¿ = m f_0(\eta_i) + \frac{\kappa}{2}\sum_{i=1}^{p} (\vec{\nabla}\eta_i)^2 \quad (2)$$

With f_0 a fourth order Landau polynomial of the order parameters, representing a homogeneous free energy of the double-well type:

$$f_0(\eta_i) = \sum_{i=1}^{p}\left[\frac{\eta_i^4}{4} - \frac{\eta_i^2}{2}\right] + \gamma\sum_{i=1}^{p}\sum_{j>i}^{p}\eta_i^2\eta_j^2 + \frac{1}{4} \quad (3)$$

Each term in the first set of summations is a double-well potential with minima located at -1 and +1 for η_i. The cross term ($\eta_i^2\eta_j^2$) was added to make it energetically unfavourable to have two order parameters different from zero at the same position in the system because it gives a positive contribution to the local free-energy density for each extra phase field variable with a value different from 0. Therefore, within the grains only one of the phase field variables differs from 0 and at a grain boundary and multi-junctions, only those phase field variables representing the adjacent grains are different from zero [31,32]. The parameter γ is taken constant and equal to 1.5 because the phase field profiles are symmetrical and cross each other at 0.5 in the interface in this case, as investigated previously by Moelans et al. [31]. With this constant value, κ_{ij} and m_{ij} define the physical properties of an interface between phases i and j, such as the interfacial energy σ_{ij} and the diffuse interface width l_{ij} [21,31]. The local values of the model parameters ($\kappa(r)$, $m(r)$ and $L(r)$ with r representing the space) are defined as a weighted sum of the interfacial parameters κ_{ij}, m_{ij} and L_{ij} [21,31,33], as illustrated for κ below:

$$\kappa(r)=\frac{\sum_{i=1}^{p}\sum_{j>i}^{p}\kappa_{ij}\eta_i(r)^2\eta_j(r)^2}{\sum_{i=1}^{p}\sum_{j>i}^{p}\eta_i(r)^2\eta_j(r)^2} \quad (4)$$

The interfacial energy σ_{ij} of the phase boundary between the phases i and j can be calculated analytically for symmetrical phase field profiles (if γ =1.5) [21,31,33]:

$$\sigma_{ij}=\frac{\sqrt{2}}{3}\sqrt{m_{ij}\kappa_{ij}} \quad (5)$$

Moreover, the interfacial width can be calculated as [21,31,33]:

$$l_{ij}=\sqrt{\frac{8\kappa_{ij}}{m_{ij}}} \quad (6)$$

The bulk energy density part of the total free energy of the system is derived from the Gibbs energies of all phases as a function of temperature and composition, $G_m(x_k,T)$, but divided by the molar volume to get the energy density per phase (f_i).

$$f_b=\sum_i h_i f_i(x_1^i,\ldots,x_k^i,\ldots,x_{C-1}^i) \quad (7)$$

The following interpolation function was used:

$$h_i=\phi_i=\frac{\eta_i^2}{\sum_i \eta_i^2} \quad (8)$$

Where η_i represents the phase field variable and ϕ_i represents the local phase fraction. Note that the local phase fractions sum up to one, but there is no restriction on the phase field variables η_i. As proposed by Kim et al. [34], every phase has its own set of composition variables x_k^i, called the phase compositions. These differ from the local composition x_k but are unambiguously defined at each point by the requirement of equal phase diffusion potentials for all components in all coexisting phases, due to the thin-interface approach, and a mass balance equation (at constant molar volume) for each component to relate the overall composition of a component *k* to the phase compositions:

$$\tilde{\mu}_k=\frac{\partial f_1(x_k)}{\partial x_k^1}=\ldots=\frac{\partial f_p(x_k)}{\partial x_k^p},\forall k \quad (9)$$

$$x_k=\sum_i h_i x_k^i \quad (10)$$

The diffusion potential of component k in phase i is defined as the difference between the chemical potential of that component and the chemical potential of a reference component (say component 0):

$$\tilde{\mu}_k = \tilde{\mu}_k^i = \mu_k^i - \mu_0^i, k = 1 \ldots c-1 \tag{11}$$

Actually, the difference between the chemical potentials of a certain component and the chemical potential of the reference component in the same phase, i.e. the diffusion potential, equals the derivative of the molar Gibbs free energy of that phase to the mole fraction. However, for constant molar volumes, an assumption usually made in phase field models, these relations are equivalent for Gibbs energies and chemical potentials per volume.

2.2 PHASE FIELD EQUATIONS

The evolution of each phase field variable is assumed to be linear with its driving force, according to the linear non-equilibrium thermodynamics theory of Onsager. Every change in the phase field variables should decrease the total energy *F* of the system. The evolution equation of η_i, is thus written as a time-dependent Ginzburg-Landau equation for non-conserved variables:

$$\frac{\partial \eta_i}{\partial t} = -L\left(m\frac{\partial f_0}{\partial \eta_i} + \frac{\partial f_b}{\partial \eta_i} - \nabla_x\left(\frac{\partial f}{\partial \nabla_x \eta_i}\right) - \nabla_y\left(\frac{\partial f}{\partial \nabla_y \eta_i}\right)\right) \tag{12}$$

Where the ∇_x and ∇_y operators are equivalent to the one-dimensional partial derivatives $\partial/\partial x$ and $\partial/\partial y$. The expansion of these terms depends on whether or not anisotropy is taken into account. For the isotropic derivation, both terms can be replaced by a single term of $-\kappa \nabla^2 \eta_i$. The anisotropic case is derived in the following section. The other terms in (12) have the following expressions:

$$\frac{\partial f_0}{\partial \eta_i} = \eta_i^3 - \eta_i + 2\gamma \eta_i\left(\sum_{j \neq i}^{p} \eta_j^2\right) \tag{13}$$

$$\frac{\partial f_b}{\partial \eta_i} = \sum_{j=1}^{p} \frac{\partial \phi_j}{\partial \eta_i}\left(f_j - \sum_{k=1}^{C-1} \tilde{\mu}_k x_k^j\right) \tag{14}$$

$$\frac{\partial \phi_j}{\partial \eta_i} = \frac{-2\eta_i \eta_j^2 + 2\delta_{ij}\eta_i\left(\sum_{r=1}^{p} \eta_r^2\right)}{\left(\sum_{r=1}^{p} \eta_r^2\right)^2} \tag{15}$$

Where δ_{ij} represents the Kronecker delta, being 1 if i=j and 0 if not. Because of the cross products, ghost fields (i.e. other phase fields than those representing the neighbouring phases but contributing at the phase boundaries) always result in an increase of the local free energy and are accordingly unstable. Therefore, expressions for the grain boundary properties derived for two-grain structures remain valid for individual grain boundaries in polycrystalline structures, except for very small grains [21].

2.3 DIFFUSION EQUATIONS

Each *C-1* independent component evolves in time according to a diffusion equation, derived from a time-dependent Ginzburg-Landau equation for conserved variables:

$$\frac{\partial x_k}{\partial t} = \nabla \cdot \left[\sum_{i=1}^{p} \phi_i \left(\sum_{l=1}^{C-1} M_{kl}^{i} \nabla \tilde{\mu}_l^i \right) \right] \tag{16}$$

where the gradients in the diffusion potential are the driving forces for multicomponent diffusion because cross-terms are included. This mobility is equivalent to the Onsager coefficient, that can be linked to the interdiffusion coefficient.

2.4 ANISOTROPY

The morphology of a growing crystal depends on the properties of the solid-liquid interface, i.e. the anisotropy of the interfacial energy and mobility. The degree of anisotropy will have a significant effect on the growth morphology and equilibrium shape of particles [35]. For two-dimensional systems, the normal to the interface $\vec{n} = (n_1, n_2)$, which is in fact the normal to contours of constant value of a phase field variable η_i, is given by

$$(n_1, n_2) = \frac{1}{\sqrt{\left(\frac{\partial \eta_i}{\partial x}\right)^2 + \left(\frac{\partial \eta_i}{\partial y}\right)^2}} \left(\frac{\partial \eta_i}{\partial x}, \frac{\partial \eta_i}{\partial y} \right) \tag{17}$$

and the angle θ between the normal to the interface between phases i and j and the x-axis is

$$\tan(\theta_{ij} - \theta_0) = \frac{\left| \nabla \eta_i - \nabla \eta_j \right|_y}{\left| \nabla \eta_i - \nabla \eta_j \right|_x} \tag{18}$$

With θ_0 a reference orientation from which the orientation of the interface is measured. When considering a single crystal orientation, the choice of θ_0 is arbitrary, as Heulens already demonstrated the rotation-invariance of the model [36]. In all simulations, it was set to zero, meaning that the orientation of the boundary is given as the angle θ_{ij} between the normal to the interface and the x-axis. For faceted crystal growth in oxide systems, the orientation dependence is characterized by strong anisotropy in the interface kinetics and thus the phase field mobility L_{ij} is incorporated to have cusps at slow growth directions that define the growth geometry of the crystal. In this model, focussing on the growth of the solids, faceted growth with sharp cusps at the facet plane orientations is described by the following orientation-function for the kinetic coefficient *L* [27]:

$$\lambda_{ij}(\theta_{ij}) = 1 - \beta_{ij} + 2\beta_{ij} \tanh\left(\frac{r_{ij}}{\left| \tan(a_{ij}\theta_{ij}) \right|} \right) \tag{19}$$

With β_{ij} a measure for the depth of the cusps (i.e. the difference in mobility between the fast and slow crystal planes), *r* the sharpness of the cusps (influencing the corner formation at the

edges of two crystal planes) and $2a_{ij}$ the mode of symmetry of the anisotropy (mostly a value of 4 or 6 for minerals such as spinel or corundum).

2.5 BOUNDARY IN CONTACT WITH ATMOSPHERE AT A CERTAIN P_{O2}

As implemented by Heulens [30] the FeO/Fe_2O_3 ratio in an FeO_x-SiO_2 melt can be linked to the local oxygen potential in the melt. If the melt is in contact with an oxygen-containing atmosphere, the melt will be oxidized or reduced, depending on whether the oxygen fugacity in the atmosphere is higher or lower than its activity in the melt. At this boundary, representing the contact with an oxygen-containing atmosphere, there is only an exchange possible for oxygen, but not for the other elements. For this, the atmosphere is assumed to be an ideal gas (thus the activity of a gaseous component equals its partial pressure and its fugacity) and diffusion is assumed to be much slower than the redox reaction, which are present in the melt when it is not in thermodynamic equilibrium with the oxygen-containing atmosphere. Moreover, the melt is assumed to be in local equilibrium with the gaseous atmosphere at the interface with the atmosphere. From these assumptions, the FeO/Fe_2O_3 ratio can be used as a direct measure for the oxygen activity within the atmosphere. However, one should note this is generally not the case. Thus, the FeO/Fe_2O_3 ratio can be varied, but the amount of Fe should remain constant. Linearly interpolating the mole fractions of FeO and Fe_2O_3 between ghost nodes and the border, together with the conservation of mass for Fe, yields the following set of equations at the boundary:

$$\left(\frac{x_{FeO}^{border}-x_{FeO}^{ghost}}{\Delta z}\right)\left(\frac{\Delta z}{2}\right)+x_{FeO}^{ghost}=\omega\left[\left(\frac{x_{Fe2O3}^{border}-x_{Fe2O3}^{ghost}}{\Delta z}\right)\left(\frac{\Delta z}{2}\right)+x_{Fe2O3}^{ghost}\right] \qquad (20)$$

$$x_{FeO}^{ghost}+2\,x_{Fe2O3}^{ghost}=x_{FeO}^{border}+2\,x_{Fe2O3}^{border}$$

With ω the FeO/Fe_2O_3 ratio determined with the help of Factsage. p_{O2} values of $2\bullet10^{-3}$ atm, $2.5185\bullet10^{-3}$ atm (the natural p_{O2} of the slag); $5\bullet10^{-3}$ atm; 10^{-2} atm and 10^{-1} atm were simulated and correspond to the following x_{FeO}/x_{Fe2O3} ratios, respectively: 1.059, 1.014, 0.891, 0.781 and 0.506. This set of equations is solved for the values of the global compositions of FeO and Fe_2O_3 in the ghost nodes for this boundary.

2.6 TABULAR COUPLING TO THERMODYNAMIC DATABASE

There is a constant drive to perform more complex simulations which would allow for quantitative kinetic predictions of microstructural evolution in multicomponent materials. Such simulations require the input of thermodynamic data. In this model, in equation (7), the bulk chemical energy density is calculated as a weighted sum of the Gibbs free energies of the different phases, f_i. However, the thermodynamic and kinetic descriptions used in phase field simulations are often simple and idealized as the use of a proper CALPHAD database would drastically increase simulation time. [37]

As summarized by Coutinho et al. [29], coupling to a thermodynamic database has been done in various ways in the past:

- The Gibbs free energy expressions, as well as the expressions for the chemical potentials and their derivatives, as a function of the composition variables are used directly. This seems a very straightforward idea and it is indeed straightforward if all phases show the behaviour of a substitutional solution.

  However, most solid phases are described using a sublattice model, for which the coupling is already called complex. Moreover, in oxidic systems, the thermodynamic functions are expressed as a function of oxide components and not as a function of the elements. Furthermore, the model for the liquid slag in the thermodynamic database for oxides (FTOxid, from Factsage) is the Modified Quasi-Chemical Model [38–40]. This model is more realistic than the ideal or regular models and looks at a random distribution of atom pairs. This results in the presence of pair fractions in the expressions of the enthalpy, entropy and hence the Gibbs energy. These pair fractions can be determined by a minimization procedure and thus, results in a globally iterative procedure. Hence, it is not possible to get one equation to describe the Gibbs energy of a liquid oxide solution described by this kind of models.

- A paraboloid expression fitted to data calculated with the CALPHAD method can also be used to approximate the composition dependence of the Gibbs free energy. This is for example used to describe stoichiometric solid phases.
  The stoichiometric phases were treated to ensure that a correct Gibbs free energy value is found at the stoichiometric composition. Moreover, all components have the same chemical diffusion potential as the solution phases from the start of the simulation onwards. Furthermore, the curvature of the parabolic Gibbs free energy should be sufficiently high (at least 10 times that of the liquid) to minimize the deviation from the expected equilibrium compositions in the coexisting solution phases and to minimize the solubility in the stoichiometric phase. Note that a too high value for the curvature will yield an ill-conditioned set of equations, which becomes unsolvable. The expression of Gibbs free energy of the stoichiometric compound as a function of the complete composition domain is described as:

$$F = \frac{A}{2} x_1^2 + \frac{B}{2} x_2^2 + \frac{C}{2} x_3^2 + D x_1 + E x_2 + F x_2 + G \qquad (21)$$

  With x_1, x_2 and x_3 the mole fractions of the components within the stoichiometric phase and x^S_1, x^z_2 and x^z_3 corresponding to the stoichiometric composition. A-G are constant for all phase concentrations. The previously mentioned constraints yield a set of equations which can provide values for these constants. Here, the chemical diffusion potential of the liquid is evaluated at a liquid composition in equilibrium with the stoichiometric phase. However, the liquid interface composition is not known before the simulation. However, Heulens et al. [19] already investigated the influence of this initial equilibrium, used to construct the paraboloid, and found that this does not affect the steady state growth of the stoichiometric phase if the paraboloid is taken at least 10 times steeper than the Gibbs energies of the solution phases. In this work, the solid precipitate is implemented as a steep parabola with the following composition (mole fractions) 0.005

Cu_2O – 0.495 FeO – 0.495 Fe_2O_3 – 0.005 SiO_2 for numerical reasons, i.e. to ensure correct phase equilibria and minimal solubility in the stoichiometric phase. The composition and description of such a solid phase was not the focus of this work and was already briefly touched Heulens et al. [19,41].
However, this paraboloid approximation can only describe the Gibbs free energy accurately over limited compositional ranges and is thus not generally usable. Moreover, for higher-order systems, the molar fractions typically start taking nonphysical fractions values below 0 or above 1.

- External software can also be used to evaluate thermodynamic quantities as required by the phase-field simulation. For the Factsage software, this is the Chemapp library [42,43]. The time spent in the communication between software is huge and is thus the main disadvantage of this approach, making it far less efficient. Some small simulation tests for such a coupling type of only 1100 and 1500 time steps took 35 and 47 days, respectively. Note, furthermore, that this programming interface typically requires a dongle to be present, which is not compatible with domain parallelization for speed-up of the simulations.
- However, this thermodynamic software can still be used for sampling the data as a function of composition and saving them into lookup tables that are consulted in the phase-field simulation. This method was first used in this work to describe the thermodynamics of the liquid phase.

With the latter method, the developed phase field model does not rely on a specific type of thermodynamic software or database. [33] The Gibbs energies of the different phases are approximated by a second-order Taylor approximation $\hat{f}_i$ around $\hat{x}^i=\left(\hat{x}_1^i,\ldots,\hat{x}_k^i,\ldots,\widehat{x_{C-1}^i}\right)$.

$$\hat{f}_i=\sum_{k=1}^{C-1}\left(\frac{A_{kk}^i}{2}\left(x_k^i-\hat{x}_k^i\right)^2\right)+\sum_{k=1}^{C-1}\left(\sum_{l>k}^{C-1}\left(A_{kl}^i\left(x_k^i-\hat{x}_k^i\right)\left(x_l^i-\hat{x}_l^i\right)\right)\right)+\sum_{k=1}^{C-1}\left(B_k^i\left(x_k^i-\hat{x}_k^i\right)\right)+ \quad (22)$$

The parameters *A*, *B* and *C* are retrieved at every concentration $\hat{x}^i$ from a thermodynamic database. The FToxid database was used to retrieve the thermodynamic data. The composition domain was first discretized on a square grid with a grid spacing of 0.005 and then *A*, *B* and *C* are calculated at every grid point as $\frac{\partial\tilde{\mu}_k^i}{\partial x_l^i}$, $\tilde{\mu}_k^i$ and $\frac{G_m^i}{V_m}$, respectively, with Chemapp [42]. This kind of multidimensional arrays are also called tensors. The order of a tensor is the number of dimensions, in this case the number of independent components. These tensors are retrieved from the thermodynamic databases before the start of the phase field simulations and the same set of thermodynamic tensors can be used to perform several phase field simulations considering the same system. So there is no need to retrieve all thermodynamic data for each phase field simulation.

Within the phase field simulation, the thermodynamic data are calculated at the local phase composition using a multilinear interpolation and the $\widehat{x_k^p}$ values of the Taylor expansion are actually the x_k^p values from the previous time step. This is in accordance with the condition for Taylor expansions that the point around which the expansion is taken, lies close enough to the point in which the actual value will be calculated.

2.7 TENSORIAL COUPLING TO THERMODYNAMIC DATABASE

The pre-calculation of thermodynamic data tensors is a feasible option to be used in phase-field simulations. However, computing all entries in these tensors becomes challenging as the number of entries grows exponentially in the order of the tensor, i.e., in the number of components. In particular, if each of the N (=C-1) independent molar fractions is equidistantly discretized into I grid points, the number of tensor entries grows exponentially as I^N. The computational difficulties caused by this exponential dependence are known as the curse of dimensionality [28]. While the number of grid points per mode can be used to reduce the number of entries and therefore the computational cost, a grid that is too coarse would negatively impact the simulation results due to the low accuracy of interpolated points.

The original thermodynamic data consisted of third-order tensors with I=201 grid points in each dimension. As molar fractions always sum to 1, only tensor entries inside a regular tetrahedron are feasible; see Figure 1. Outside this tetrahedron, the sum of the molar fractions is greater than 1 by construction. For the thermodynamic data tensors studied in this paper, the distance between grid points is 0.005 which is chosen to provide sufficient accuracy while keeping memory requirements feasible. This way, ten tensors with dimensions 201×201×201 are obtained: one for Gibbs energy, three for diffusional potentials and six for the derivatives of the diffusional potentials. Each tensor contains already 1 373 700 feasible entries. Thus, it is clear that scanning the complete compositional domain would become impractical for larger numbers of components.

To make working with fine grids and many components feasible, the curse of dimensionality has to be broken. To achieve this, we follow the strategy outlined in Coutinho et al. [29], where thermodynamic databases are coupled and used in phase field simulations for liquid Ag-Cu-Ni-Sn alloys. Instead of using all entries inside the feasible tetrahedron in each tensor, a limited amount of entries is sampled randomly, and a constrained canonical polyadic decomposition (CPD) of the resulting incomplete tensor is computed. This way, the temperature-dependent Gibbs energy, the potentials and their derivatives were modelled over the entire composition domain without loss in simulation accuracy [29]. Vervliet et al. [28]. used a similar method to accurately model the melting temperature of a ten-compound alloy using only 100 000 samples, while approximately 10^{18} samples would be required when using all data in a naive way.

A polyadic decomposition (PD) writes a tensor as a sum of R rank-1 terms, each of which is an outer product of N non-zero factor vectors $a_r^{(n)}$. These factor vectors can be collected into factor matrices: $A^{(n)}=[a_1^{(n)}, a_2^{(n)}, \ldots, a_R^{(n)}]$. Mathematically, each entry of a tensor T is given by:

$$t_{i_1 i_2 \ldots i_N} = \sum_{r=1}^{R} a_{i_1 r}^{(1)} a_{i_2 r}^{(2)} \ldots a_{i_N r}^{N} \tag{23}$$

If R is minimal, the decomposition is called canonical, hence the nomenclature 'CPD'. Compared to matrix decompositions, the CPD is unique under mild conditions which is useful in applications where terms are interpreted or when having a single best solution is required; (see [44] for more detail). Additional constraints can be imposed onto the factor matrices. In this paper, we assume that each factor can be written as the matrix product of a known basis matrix $B^{(n)}$ and an unknown coefficient matrix $C^{(n)}$, i.e., $A^{(n)} = B^{(n)}C^{(n)}$. This CPD with linearly constrained factors can be computed efficiently from incomplete tensors, i.e., tensors have only few sampled entries [45].

Each thermodynamic data tensor contains samples from an underlying smooth multivariate function in the molar fractions $f(x_1, x_2, \ldots, x_N)$. In this paper, we follow [29,45] by modelling this function by a sum of separable functions, which are the product of functions in a single variable:

$$f(x_1, x_2, \ldots, x_N) = \sum_{r=1}^{R} a_r^{(1)}(x_1) a_r^{(2)}(x_2) \ldots a_r^{N}(x_N) \tag{24}$$

This is exactly the continuous variant of equation (25). By expressing these univariate functions as the sum of basis functions $b_d^{(n)}(x_n)$, e.g., for a monomial basis $b_d^{(n)}(x_n) = x_n^d$, d=0,..., D, with D the maximal degree and by sampling the function on a grid, the formulation of a CPD with linearly constrained factors is obtained: the j^{th} row in $A^{(n)}$ contains the R univariate functions $a_r^{(n)}$ evaluated at the j^{th} grid point for x_n, and each $a_r^{(n)} = \Sigma\, b_d^{(n)}(x_n)\, c_{dr}^{(n)}$, i.e., the product of the evaluated basis functions and some coefficients $c_{dr}^{(n)}$. As the basis functions are chosen beforehand, only the coefficients collected into D×R matrices $C^{(n)}$, need to be computed, e.g., using the algorithm in [45].

Using a CPD, a continuous model for the entire domain is obtained, which has several advantages. In contrast to local quadratic interpolation, there is no need to have a small distance between grid points and hence sampling on a fine grid is not needed. Moreover, by strategically placing more samples in regions where the function varies a lot, e.g., at the boundaries of the interval, the number of samples can be reduced significantly. Once the coefficient matrices $C^{(n)}$ have been found, the function value can be obtained for every point in the domain by evaluating the basis functions at the desired molar fractions, computing $A^{(n)}=B^{(n)}C^{(n)}$and using equation (25). Finally, the relation between Gibbs energy, diffusion potentials and its derivatives can be exploited by replacing a basis function with its derivative. From equation (26), it is clear that the derivative with respect to x_1 only affects $a_j^{(1)}(x_1)$ and not $a_j^{(n)}(x_n)$ for $n \neq 1$. Moreover, as only $B^{(1)}(x_1)$ depends on x_1, the coefficient matrix $C^{(1)}$ does not change. Therefore, the different thermodynamic data tensors can analyzed together by coupling the coefficient matrices $C^{(n)}$; see [29] for more details.

In this paper, we investigate whether this approach outlined in [29] for liquid alloys is feasible here as well. In oxidic systems, however, the dependence on the molar fractions is far more intricate, not only because of the consideration of the oxidic components instead of the

elements, but also the more intricate nature of the Modified Quasi-chemical Model, which describes the liquid slag.

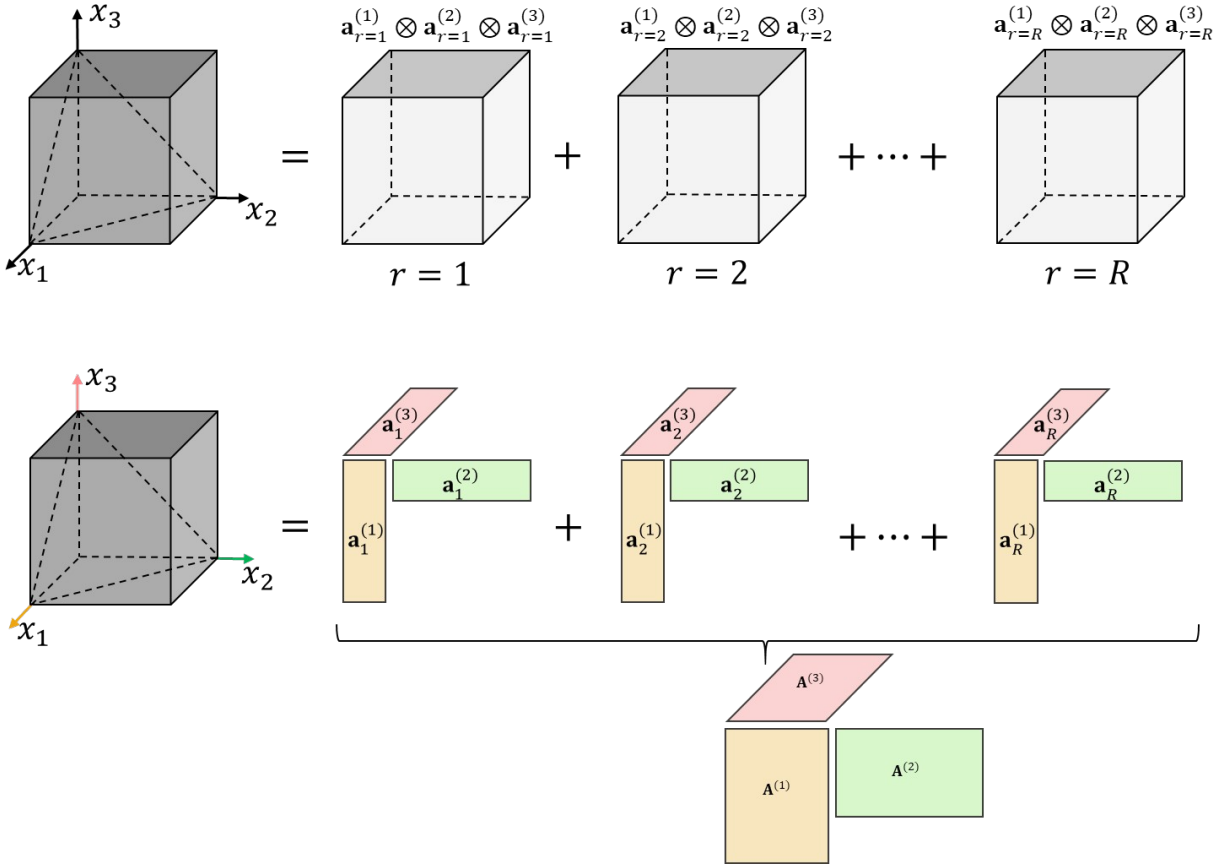

Figure 1 Visualisation of a canonical polyadic decomposition (CPD), adapted from [29]

3 NUMERICAL METHODS

The numerical implementation of this model was done in Fortran 90. The system is divided into a two-dimensional grid with equal distances between grid points in both the x- and y-axis. The evolution equations for both the conserved and non-conserved field variables are solved with spatial central finite differences and temporal forward finite differences. To be able to account for different boundary conditions for the system, ghost nodes were introduced next to the outer rim of the system grid points.

The program starts by reading the input and initializing the system. Then a loop considers the evolution over the various time steps and in every time step, the following happens:

- Computation of the phase fractions ϕ_i from its definition and the computation of the phase compositions x_k^p from the mass balance equation and the quasi-equilibrium condition.

- Computation of the local $\kappa(r)$, $m(r)$ and $L(r)$ values. For this, first the interface angle is determined and the gradients herein are calculated with a higher accuracy nine-point stencil:

$$\begin{aligned}\nabla_x \eta_{ri,j} &= \frac{1}{8}\left(\frac{\eta_{ri+1,j-1}-\eta_{ri-1,j-1}}{2\Delta x}\right)+\frac{6}{8}\left(\frac{\eta_{ri+1,j}-\eta_{ri-1,j}}{2\Delta x}\right)+\frac{1}{8}\left(\frac{\eta_{ri+1,j+1}-\eta_{ri-1,j+1}}{2\Delta x}\right)\\ \nabla_y \eta_{ri,j} &= \frac{1}{8}\left(\frac{\eta_{ri-1,j+1}-\eta_{ri-1,j-1}}{2\Delta y}\right)+\frac{6}{8}\left(\frac{\eta_{ri,j+1}-\eta_{ri,j-1}}{2\Delta y}\right)+\frac{1}{8}\left(\frac{\eta_{ri+1,j+1}-\eta_{ri+1,j-1}}{2\Delta y}\right)\end{aligned} \quad (25)$$

  This nine-point stencil is required to reduce the effect of the grid anisotropy and provide a stable solution for the orientation dependence. The orientation dependence for the phase field mobility is implemented with a weighed sum between the isotropic mobility and faceted growth (interface controlled growth) according to (19).
- Computation of f_i and $\tilde{\mu}_k^i$ at the local phase concentrations using a bilinear interpolation between the values of C and B, respectively, which were tabulated.
- Computation of the phase field and concentration gradients.
  - The temporal differential in the diffusion equations is discretized with a forward finite difference, i.e. the mole fraction at time step n+1 is calculated with the values of the previous time step n. The gradient can also be split up into its two components, yielding:

$$\left(x_k\right)_{i,j}^{n+1} = \left(x_k\right)_{i,j}^{n} + \Delta t\left(\nabla\cdot\left[\sum_{i=1}^{p}\phi_i\left(\sum_{l=1}^{C-1}M_{kl}^{i}\left(\nabla_x\tilde{\mu}_l^i+\nabla_y\tilde{\mu}_l^i\right)\right)\right]\right)^n \quad (26)$$

  These gradients are discretized as:

$$\left(x_k\right)_{i,j}^{n+1} = \left(x_k\right)_{i,j}^{n} + \Delta t\left(\frac{\xi_{x,i,j}^{n}-\xi_{x,i-1,j}^{n}}{\Delta x}+\frac{\xi_{y,i,j}^{n}-\xi_{y,i,j-1}^{n}}{\Delta y}\right) \quad (27)$$

  With

$$\begin{aligned}\xi_{x,i,j}^{n} &= \left[\sum_{i=1}^{p}\frac{\left(\phi_i\right)_{i+1,j}^{n}+\left(\phi_i\right)_{i,j}^{n}}{2}\left(\sum_{l=1}^{C-1}M_{kl}^{i}\frac{\left(\tilde{\mu}_l^i\right)_{i+1,j}^{n}-\left(\tilde{\mu}_l^i\right)_{i,j}^{n}}{\Delta x}\right)\right]\\ \xi_{y,i,j}^{n} &= \left[\sum_{i=1}^{p}\frac{\left(\phi_i\right)_{i,j+1}^{n}+\left(\phi_i\right)_{i,j}^{n}}{2}\left(\sum_{l=1}^{C-1}M_{kl}^{i}\frac{\left(\tilde{\mu}_l^i\right)_{i,j+1}^{n}-\left(\tilde{\mu}_l^i\right)_{i,j}^{n}}{\Delta y}\right)\right]\end{aligned} \quad (28)$$

  - The gradients in the phase field equations were computed in a more elaborate way to take the anisotropy correctly into account. The temporal differential is discretized with a forward finite difference, i.e. the phase field at time step n+1 is calculated with the values of the previous time step n, yielding:

$$\left(\eta_r\right)_{i,j}^{n+1}=\left(\eta_r\right)_{i,j}^{n}+\Delta t\left[-L\left(m\frac{\partial f_0}{\partial \eta_r}+\frac{\partial f_b}{\partial \eta_r}-\frac{\xi_{x,i,j}^{n}-\xi_{x,i-1,j}^{n}}{\Delta x}-\frac{\xi_{y,i,j}^{n}-\xi_{y,i,j-1}^{n}}{\Delta y}\right)\right]^{n} \quad (29)$$

The first two terms in the large brackets are evaluated at time step n. The last two terms in the large brackets are the gradient parts of the phase field equation and are numerically solved according to equation (20)Error: Reference source not found.Moreover, ξ in equation (31) is defined as

$\xi_{x,i,j}^{n}=¿$

With $\nabla_x\eta_r=\frac{1}{8}\left(\frac{\left(\eta_r\right)_{i+1,j+1}^{n}-\left(\eta_r\right)_{i,j+1}^{n}}{\Delta x}\right)+\frac{6}{8}\left(\frac{\left(\eta_r\right)_{i+1,j}^{n}-\left(\eta_r\right)_{i,j}^{n}}{\Delta x}\right)+\frac{1}{8}\left(\frac{\left(\eta_r\right)_{i+1,j-1}^{n}-\left(\eta_r\right)_{i,j-1}^{n}}{\Delta x}\right)$ (30)

and $\nabla_y\eta_r=\left(\frac{\left(\eta_r\right)_{i,j+1}^{n}+\left(\eta_r\right)_{i+1,j+1}^{n}-\left(\eta_r\right)_{i,j-1}^{n}-\left(\eta_r\right)_{i+1,j-1}^{n}}{4\Delta y}\right)$

and θ_{rs} determined with these gradients.

An analogous expression for $\xi_{y,i,j}^{n}$ was used; The only difference is that the numerators in the first two terms contain $+\left(\nabla ¿¿x\eta_r-\nabla_x\eta_s\right)¿$ instead of $-\left(\nabla ¿¿y\eta_r-\nabla_y\eta_s\right)¿$.

- Step evolution in the phase field and diffusion equations. The phase field equations are only solved in proximity of interfaces to increase the numerical efficiency, while the diffusion equations are solved everywhere.
- Updating the values of the conserved and non-conserved variables on the ghost nodes according to the boundary conditions (no-flux or for the conserved variable: corresponding to an atmosphere with a certain p_{O2}).

4 INPUT PARAMETERS

In this work, the diffuse interface between the liquid slag and the solid spinel equals $l_{12} = 10^{-7}$ m. The interface contains eight grid points, yielding a system discretization with $\Delta x = 0.125 \cdot 10^{-7}$ m. The size of the time discretization is restricted by stability of the diffusion equations and equals $\Delta t = 2.0 \cdot 10^{-7}$ s. To obtain the interface width, the following model parameters were used: $\sigma_{12} = 0.225 \cdot 10^{-7}$ J/m and $m_{12} = 1.8 \cdot 10^{7}$ J/m³, according to the following equation

$$l_{ij}=\sqrt{\frac{8\kappa_{ij}}{m_{ij}}} \quad (31)$$

Moreover, the next equation gives the relation between the model parameters and the interface energy.

$$\sigma_{ij} = \frac{\sqrt{2}}{3}\sqrt{m_{ij}\kappa_{ij}} \tag{32}$$

This yields an interface energy of σ_{12} = 0.3 J/m². The molar volume was calculated from literature previously [30,33]: $V_m = 23.6 \cdot 10^{-6}$ m³/mol.

The mobilities are calculated based on the diffusion coefficients and the thermodynamic factors. The most elaborated mobility databases nowadays are part of the DICTRA software package and include data for iron, nickel, aluminium, titanium and silicon based alloys, but no kinetic database has been developed yet for oxide systems. [46] Therefore, we used the previously [30] determined mobilities for FeO and Fe_2O_3, estimated from literature for a Fe_2O_3-CaO-SiO_2 melt at 1400°C [47], where CaO is replaced by FeO. To find a diffusion coefficient for Cu_2O in the slag, the Stokes-Einstein equation was used as an estimation. The ionic radii of the different cations can be used as an inverse measure for the diffusion coefficient [48]: Cu^+ has 0.077 nm as ionic radius, Fe^{2+} 0.070 nm and Fe^{3+} 0.060 nm. Despite the fact that the Fe^{3+} ion has a smaller ionic radius, it has a lower diffusion coefficient than Fe^{2+} [49], because a larger valence number will yield slower diffusion. Thus, the following values were used for the mobilities in the slag: $M_{Cu2O\text{-}Cu2O} = 0.02 \cdot 10^{-19}$ m^5/ (J s); $M_{FeO\text{-}FeO} = 0.1 \cdot 10^{-19}$ m^5/ (J s) and $M_{Fe2O3\text{-}Fe2O3} = 0.05 \cdot 10^{-19}$ m^5/ (J s).

For the mobilities in the solid, the same order of magnitude as in the liquid was used to avoid solute trapping effects and the off-diagonal elements of the mobility matrix were set to zero. In this respect, it should be noted that Liu et al. [50] observed that the mobility matrix of the solid does not affect the growth of that solid, because there is no diffusion in the solid as the solid crystallizes with its equilibrium composition. The kinetic coefficient L_{12} was chosen to ensure diffusion-controlled growth, as obtained by the following equation

$$L_{crit} = \frac{4 m_{ij}}{3 \kappa_{ij} \zeta} \tag{33}$$

Where

$$\zeta = \sum_{k=1}^{C-1} \left(x_{slag,eq,k} - x_{stoich,eq,k} \right) \sum_{m=1}^{C-1} m_{km} \left(x_{slag,eq,m} - x_{stoich,eq,m} \right) \tag{34}$$

With m_{km} the elements of inverse of the diffusion mobilities matrix (which contains the averages of the two mobility matrices). L_{crit} in this case is $4.1779 \cdot 10^{-5}$. If $L_{12} = L_{crit}$, the growth is diffusion-controlled; If $L_{12} < L_{crit}$, the eta-profiles will move slower than the composition profiles and if $L_{12} > L_{crit}$, the composition profiles will be slower than the eta-profiles. However, anisotropy is also present in the kinetic coefficient according to the following equation [27]:

$$L_{ij} = \overline{L_{ij}} \left(1 - \beta_{ij} + 2 \beta_{ij} \tanh \left(\frac{r_{ij}}{\left| \tan \left(a_{ij} \theta_{ij} \right) \right|} \right) \right) \tag{35}$$

With β_{ij} a measure for the depth of the cusps (i.e. the difference in mobility between the fast and slow crystal planes), r the sharpness of the cusps (influencing the corner formation at the

edges of two crystal planes) and $2a_{ij}$ the mode of symmetry of the anisotropy (mostly a value of four for spinel minerals). Moreover, $\overline{L_{ij}}$ should be calculated in such a way that the value of L_{12} for the fast moving/faceted interfaces equals L_{crit}. In this case, $\overline{L_{ij}}$ should be $2.7853 \bullet 10^{-5}$. Moreover, a_{ij} = 2 to yield a 4-fold crystal growth symmetry and β_{ij} = 0.5 to give a sufficiently high difference between the fast growing (faceted) interfaces and the slow interfaces.

The simulations are executed for a 100 x 100 domain (= 1.25 × 1.25 µm²) for 10^6 time steps (= 0.2s). The solid was initialised at its equilibrium composition (0.005 Cu_2O – 0.495 FeO – 0.495 Fe_2O_3 – 0.005 SiO_2) and the slag started as a supersaturated oxide mixture (0.1 Cu_2O – 0.4 FeO – 0.4 Fe_2O_3 – 0.1 SiO_2). According to Factsage such a supersaturated slag should decompose into solid spinel and a slag with the equilibrium composition of 0.151 Cu_2O – 0.354 FeO – 0.344 Fe_2O_3 – 0.151 SiO_2.

For the two-dimensional isotropic simulations, the system is initialized with one quadrant of a circle with a radius of 12 grid points in the lower left corner, hence focussing on $1/4^{th}$ of a solid particle. This configuration with the nucleus in the lower left corner of the system is representative for a 200x200 system due to symmetry. The presence of this initial quadrant influences the phase fractions expected from the thermodynamic calculations with the Factsage software to a minor extent, but does not influence the expected equilibrium concentrations.

The description of the stoichiometric phase ensured that the diffusion potential is the same as for the equilibrium composition of the slag. However, the thermochemical software Factsage considers formation of a solid spinel with a composition of FeO.Fe_2O_3 (also known as magnetite Fe_3O_4). Numerical reasons in the phase field simulations require the solid to be described by a slight shift away from the edge of the compositional domain. Hence, the solid in the phase field simulations contains a minor amount of Cu_2O and SiO_2. This shifts the parabola describing this phase away from the edge of the compositional domain, but this in turn has a slight effect on the equilibrium fractions and compositions. In this work, the solid precipitate is implemented as a steep parabola with the following composition (mole fractions) 0.005 Cu_2O – 0.495 FeO – 0.495 Fe_2O_3 – 0.005 SiO_2 to ensure numerical soundness in the phase field method and minimal solubility in the stoichiometric phase.

The thermodynamic data of the slag were extracted from the database with Chemapp with a discretization of 0.005 in the compositional domain. A smaller discretization resulted in encountering memory limits during the phase field simulation when the thermodynamic data is loaded in a first stage of the calculation.

5 RESULTS AND DISCUSSION

5.1 ISOTROPIC GROWTH OF SPINEL IN QUATERNARY OXIDE SYSTEM

A first simulation was performed assuming isotropic interfacial energy, using the standard value $L_{12} = 4.1779 \bullet 10^{-5}$, so that no facets are expected to form. The contours of the 0.5-level of the

solid in the system domain for every 100 000th time step are shown in Figure 2, as well as the phase fraction as a function of time.

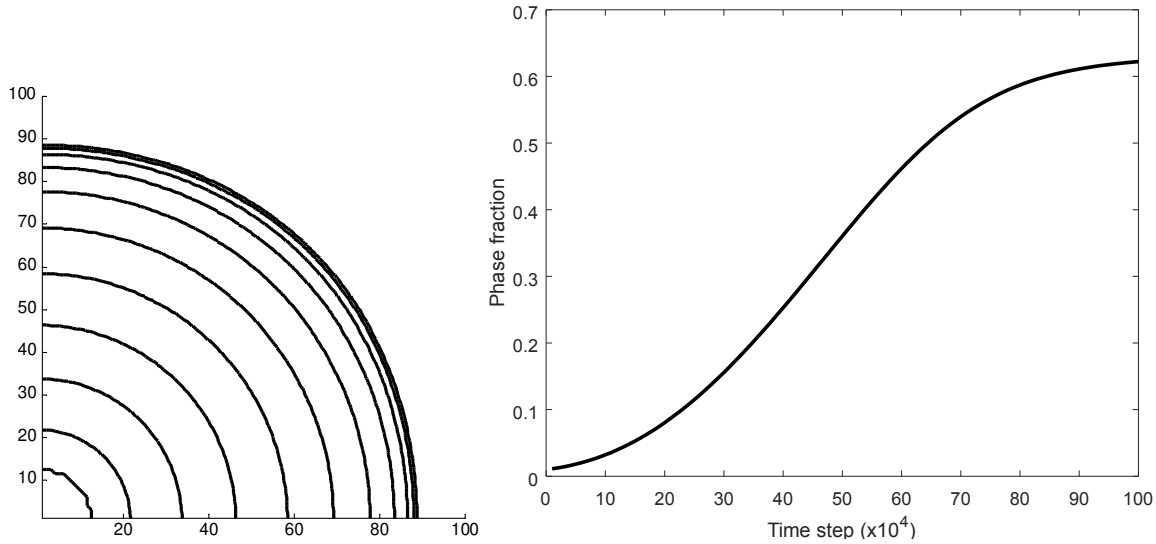

Figure 2 Left: Contours of the 0.5-level of the solid in the system domain for every 100 000th time step in a 2D-simulation with isotropic growth kinetics for the solid phase. Right: Phase fraction of the isotropic growth as a function of time.

The last couple of contours are clearly located closer together than the first contour lines. The corresponding concentration profiles of Cu_2O, FeO and Fe_2O_3 at a height of 10 grid points are shown in Figure 3.

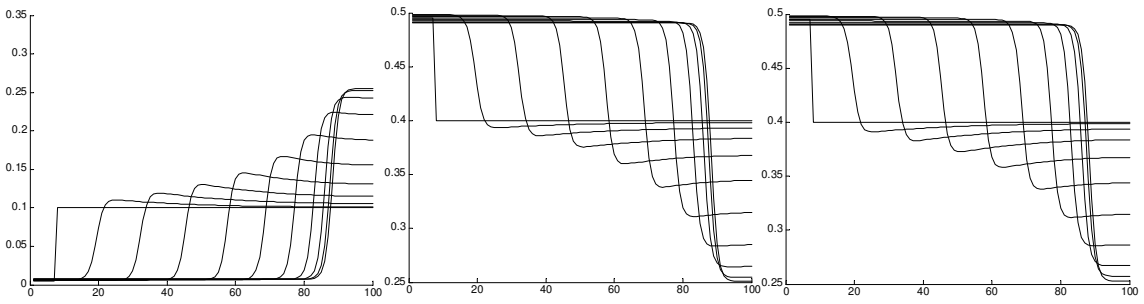

(a) x_{Cu2O} (b) x_{FeO} (c) x_{Fe2O3}

Figure 3 Concentration profiles for every 100 000th time step in the x-direction of the system domain in a 2D-simulation with isotropic growth kinetics for the solid phase.

As the spinel solid grows, the slag is enriched in Cu_2O: the concentration goes from 0.1 to more than 0.25. The FeO and Fe_2O_3 profiles are very similar, except for a slightly faster diffusion in the slag of FeO. In the concentration profiles, it also becomes apparent that the last couple of lines lay closer to each other than the first. A reason for this slower movement of the interface after a while is probably the fact that the slag gets saturated with Cu_2O and depleted in the iron oxides.

5.2 FACETED GROWTH OF SPINEL IN QUATERNARY OXIDE SYSTEM

For the faceted growth of the solid spinel phase, several r-values in the anisotropy function, determining the sharpness of the cusps in the kinetic factor, were used. The corresponding polar plots are shown in Figure 4. A larger r will yield only a limited range of angles at which the growth is slower, due to a lower L_{12}-value. A smaller r-value, on the other hand, has a larger range of angles at which the growth is slower. Thus, a larger r-value clearly would result in 'rounder' corners of the spinel particle, but faster overall growth.

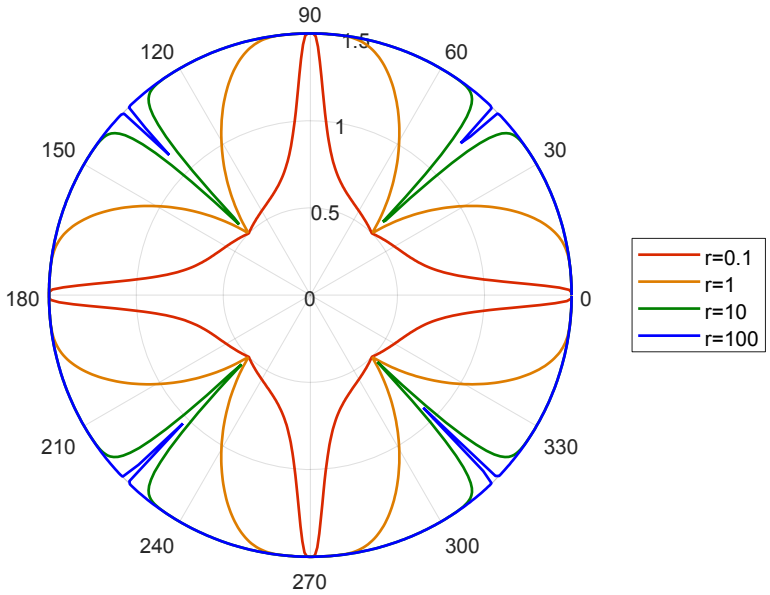

Figure 4 Polar plot of anisotropy function for four r -values with β_{ij} =0.5 and a_{ij}=2

With r = 1, for example, it is expected from the plot in Figure 4 that the corners of the spinel solids are not too round. The results of the simulations as contour plots and as phase fractions as a function of time for r = 0.1, 1, 10 and 100 are shown in Figure 5.

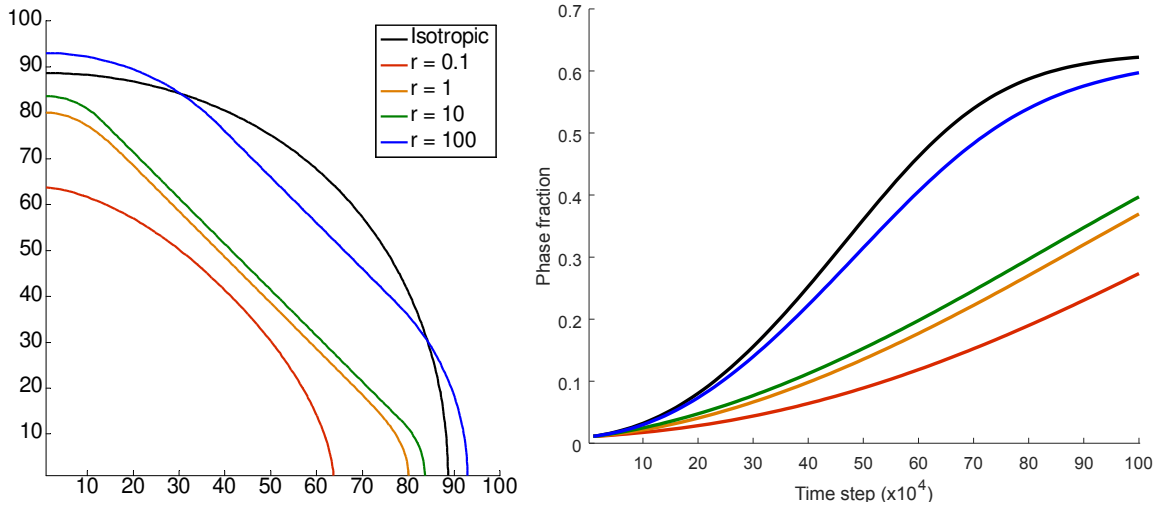

Figure 5 Left: Contours of the 0.5-level of the solid in the system domain at the final time step in a 2D-simulation assuming strong anisotropy in the solid-liquid interface kinetics with r = 0.1, 1, 10 and 100, resulting in faceted growth of the solid phase. Right: Phase fractions of the isotropic and anisotropic growth as a function of time.

It is clear from the contour plot that the growth of the spinel solid was slower than without the faceted growth. Because the anisotropy is added to the kinetic coefficient L_{12}, the fastest moving interfaces have an angle of 0 or 90° with the x-axis. The slowest moving interfaces are located at an angle of 45°. But even the fastest moving interface positions, corresponding to the x- and y-direction, are slower than the non-faceted interface movement. It seems as if the slower moving interfaces at 45° restrict the fast movement of the well-oriented interfaces. For a larger r-value, i.e. a sharper cusp in the anisotropy plot, the growth is less limited than for the r=1-case. This is because the kinetic coefficient is limited for only a very small range of angles around 45°, resulting in slower growth in that direction. For an even larger r-value, the growth seems to be even faster as compared to the isotropic growth in the fast-growing directions of 0 and 90°.

The way the spinel grows is determined by the anisotropy in the kinetic coefficient L_{12}, but the final form of the solid is determined by the interfacial energy. In these simulations, the growth of the solid particles was mainly investigated and thus, no anisotropy was used for the interfacial energy (through the parameters m and κ). The r-value, which was varied in these simulations, influences the range of angles for which the kinetic coefficient will be at its maximum value of L_{crit}. A larger r will yield only a limited range of angles at which the growth is not favoured, due to a lower L_{12}-value. Thus, a larger r-value clearly results in 'rounder' corners of the spinel solid, but faster growth, which was clearly observed in the simulations. In experiments, both the sharp and round corners can be observed as illustrated in Figure 6. Note that the presence of multiple solids was investigated by Heulens et al. [30] and that the current work focussed on a single solid particle and phase and that we investigated 1/4th of it.

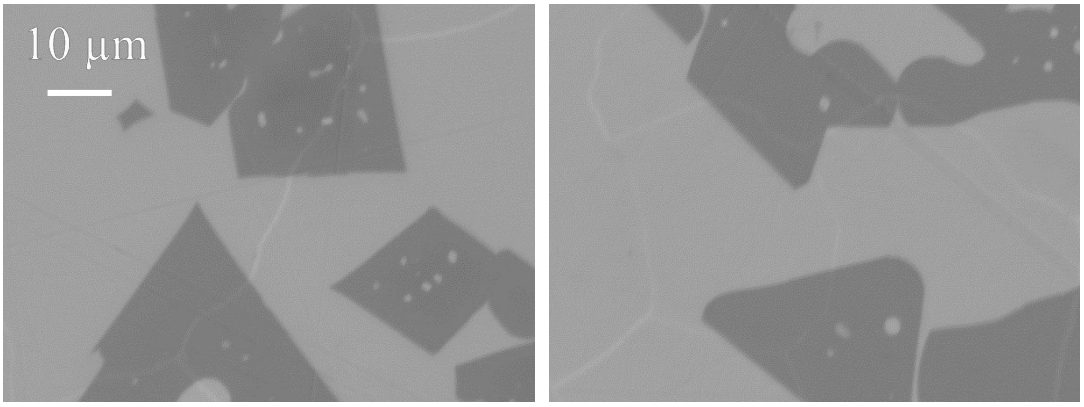

Figure 6 SEM micrographs of an experimentally obtained microstructure of solid oxide particles in a slag that was quenched to 'freeze' its high temperature condition [51–53]

The rounded corners also appear in the experimental system, but the sharp corners in the experiments are much sharper than for the simulations with the lowest r-value. These could

probably be obtained with a simulation considering a different kind of anisotropy in the interface mobility.

5.3 INFLUENCE OF P_{O2} ON FACETED GROWTH OF SPINEL IN SYSTEM WITH OPEN BOUNDARY

It is generally accepted that the chemical activity of oxygen, i.e. the oxygen fugacity, may control the oxidation state of iron in liquid oxide mixtures and thus can influence the phase equilibria, rheology and density [54,55]. At the upper boundary of the system, a certain p_{O2} is fixed, which can be implemented by imposing a certain x_{FeO} over x_{Fe2O3} ratio. This ratio is determined by the p_{O2} and can be obtained using Factsage.

The equilibrium composition of the slag (0.151 Cu_2O – 0.354 FeO – 0.344 Fe_2O_3 – 0.151 SiO_2) has a 'natural' p_{O2} of $2.5185 \cdot 10^{-3}$ atm or $10^{-2.60}$ atm, i.e. this is the partial pressure of oxygen in the gas phase that would not result in any oxidation or reduction of the slag phase. Several simulations with various p_{O2}-values at the upper boundary of the system were executed. Faceted growth of the spinel solid through anisotropy in the kinetic coefficient was used with an r-value of 10. p_{O2} values of $2 \cdot 10^{-3}$ atm, $2.5185 \cdot 10^{-3}$ atm (the natural p_{O2} of the slag); $5 \cdot 10^{-3}$ atm; 10^{-2} atm; 10^{-1} atm were simulated. The resulting contour plots and phase fractions as a function of time for these different boundaries, can be found in Figure 7.

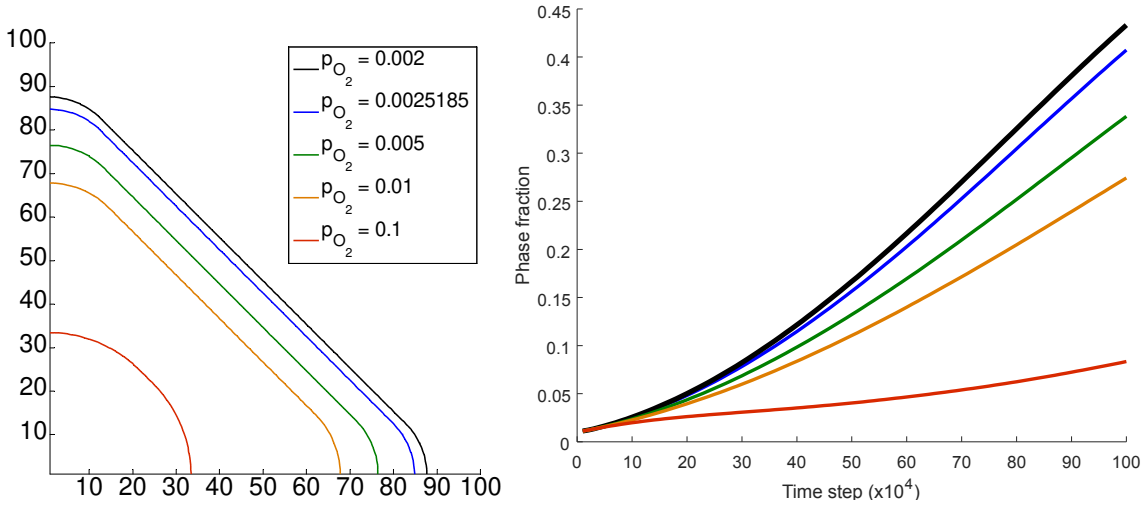

Figure 7 Left: Contour plots of the 0.5-level for the final time step in the system domain in a 2D-simulation assuming strong anisotropy in the solid-liquid interface kinetics with r=10, resulting in faceted growth of the solid phase, for several p_{O2}-values at the upper boundary Right: . Phase fractions as a function of time

A decreasing p_{O2} clearly yields faster growth. As the partial pressure of oxygen increases, the concentration of FeO and Cu_2O at the bottom of the system decreases, whereas the concentration of Fe_2O_3 increases, as is expected by the imposed boundary condition on the upper boundary. Previous results of Heulens [33] also showed that the crystallization of a ternary melt (with two possible oxidation states for Fe) has a larger effect on the oxidation state than the oxygen fugacity of the atmosphere. Furthermore, the growth velocities of the spinel crystals increase with decreasing oxygen fugacity. However, their results were for simulation

times of 10^5 time steps. In this study, we conducted 10 times longer simulations, indicating very clearly the influence of the oxygen atmosphere on the growth of the spinel solid and possible inhibition of this growth by the p_{O2}-value.

5.4 More efficient thermodynamic database coupling: canonical polyadic decomposition of tensors

In this paper, we investigate whether the use of the canonical polyadic decomposition for the thermodynamic data tensors, as outlined in [29] for liquid alloys, is feasible in oxidic systems as well. In such systems, however, the dependence on the molar fractions of the oxidic components are considered instead of the elements and furthermore, the Modified Quasi-chemical Model, describing the liquid slag, has a far more intricate nature. Two approaches of the canonical polyadic decomposition have been tested and compared to the previously used tabulation method for coupling to a thermodynamic database.

First, a fourth-order tensor is created for each of the ten datasets by using both the independent and dependent molar fractions as modes of a tensor, resulting in ten 201×201×201×201 tensors with of which we sampled between 50 000 and 100 000 entries per tensor. A more involved sampling procedure had to be used compared to [29]: we selected all points close to boundaries, i.e., for which any $x_n \leq 0.01$, and then sampled an additional 10 000 points per tensors. Then a logarithmic term of the form $R_T T \Sigma x_n \log(x_n)$, with R_T the universal gas constant and T the temperature, or the derivatives thereof is subtracted, and the data is normalized. For each of the resulting tensors, a CPD with R=10 terms is computed using Tensorlab [56] and the CPDLI NLS function [45] (All parameters are determined using validation data). The same monomial basis functions $1, x, x^2, x^3, \ldots, x^6$ and the function xlog(x) are used to form the basis matrix $B^{(n)}=B$ for each n. As a result, four factor matrices of size 201×10 are obtained by evaluating the result on an equidistant grid with steps 0, 0.005, 0.010,…,1. This way, all datasets can be described compactly using 10·4·201·10 = 80400 values in the factor matrices, while the original data required storage for 13 737 000 values.

Second, third-order tensors were created from Gibbs energy and the diffusion potentials using only the independent molar fractions. A coupled model similar to [29] was computed, with the sampling strategy outlined above and additional normalization steps. We used R=10 rank-1 terms per tensor and monomials up to degree 6 as well as a xlogx term. As a result, three coefficient matrices $C^{(n)}$ containing only 3·8·10=240 values in total were obtained. From these coefficient matrices, we again created factor matrices $A^{(n)}$ for each tensor. Using the coupled approach, we therefore can represent all data using only 10·3·201·10 = 60300 values, or 240 values if only coefficients are stored. Note that the number of values that need to be stored only increases linearly in the number of components, which makes this approach feasible for many-component systems.

For both approaches, the error relative to the range of the data is computed for each point in the original dataset, i.e., containing both training and validation data, and subsequently the 99% quantile is taken. For the Gibbs energy, the models achieve an accuracy of at least 0.4% for 99%

of the points, while the accuracy is 4% for the potential data. The points with the largest errors are located at the domain boundaries, which is expected due to the presence of logarithmic terms and their derivatives which quickly become large near zero.

Furthermore, the decomposition data were used as input for the phase field model to investigate the influence on the final microstructure. For this purpose, the growth of solid Fe_3O_4 within a supersaturated liquid was simulated in a smaller 20x20 system. Starting from a solid nucleus on the left hand side of the system, i.e., a quasi-1D system. The comparison of the phase fractions resulting from the original tensorial data and the decomposed data sets is shown in Figure 8. It is clear that the correspondence is very good.

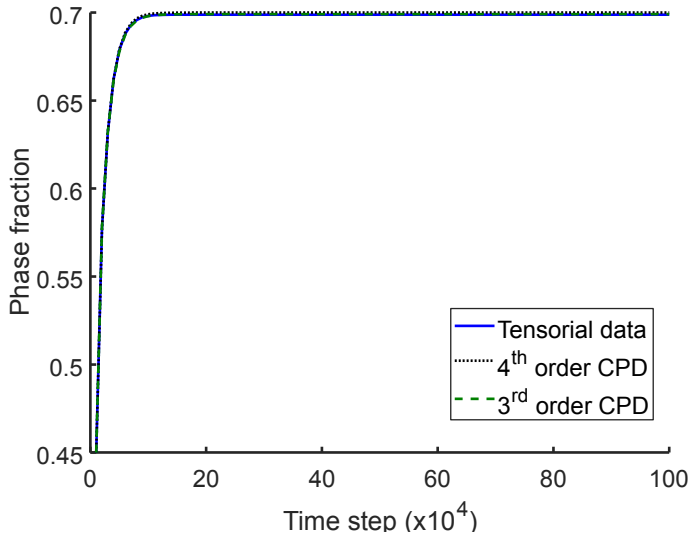

Figure 8 Comparison of phase fractions as a function of time for the growth of solid Fe_3O_4 in a super-saturated liquid slag from phase field simulations using the original tensorial dataset (10 tensors with 1 373 700 feasible entries each) and the decomposed data sets (4^{th} order CPD has 10 times 8040 input data values and the 3^{rd} order CPD has 10 times 6030 input data values)

6 CONCLUSIONS AND FUTURE WORK

To our knowledge, this is the first time that a realistic quaternary oxide system was modelled. We investigated the faceted growth and how the depth of the cusps in the anisotropy of the kinetic coefficient, influences the faceted growth of the spinel and the concentration levels within the remaining slag. Comparison to experimentally observed microstructures for solid spinel particles, however, showed that only anisotropy for the kinetic coefficient probably does not suffice to obtain completely similar microstructures of the solid particles. Moreover, the upper boundary was set to be in contact with an atmosphere with a certain p_{O2}. This illustrated that an oxidative p_{O2}-value can inhibit the growth of the solid spinel particle.

We also showed that we can obtain an extremely compact but still accurate representation of the composition dependence of thermodynamic quantities, and that the decomposed tensor representation can be used effectively in microstructural simulations. The number of

coefficients and the computational cost to evaluate a CPD depend only linearly on the number of components in the system, in contrast to an exponential increase of the amount of thermodynamic data represented. It is, however, not fully clear whether the addition of more elements will lead to a substantial increase of the complexity for oxidic systems. This technique will allow for more realistic simulations of solidification or dissolution in oxidic systems, which is relevant for refractory degradation, freeze lining, etc.

An alternative would be to start from incomplete tensors. In this case, for oxidic systems, the sampling for data points should happen carefully and with more attention than the metallic systems, due to the special behaviour near the edges. Also, if sharp transitions are expected, extra sampling points should be taken there to describe the behaviour in those regions correctly. Unfortunately, such sharp transitions are not always known beforehand, making it still required to sample almost the full compositional domain.

Note that not only the number of data points increases as the number of components increases, also the equilibrium calculations with the thermodynamic software will take longer as the number of components becomes higher. This was illustrated by Roos and Zietsman [57] and is also shown in Figure 9.

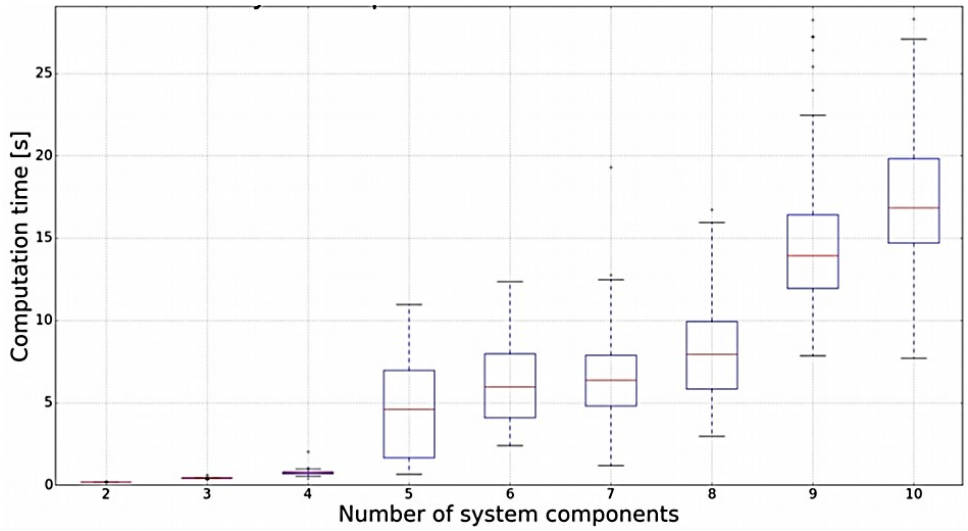

Figure 9 Non-linear relationship between the number of system components and a single equilibrium calculation's solving time. [57]

Until now, we mainly focused on thermodynamic data coupling. But note that to obtain more realistic simulations in oxidic systems, we also need extra information on different types of kinetic data:

- Diffusion data: at the moment we used orders of magnitude for the diffusion coefficients, because there is not much diffusion data available for oxidic systems.
- To investigate the influence of the partial pressure of oxygen, also more data on the ratios of Fe^{3+} over Fe^{2+} [58,59] are very relevant in various slag matrices.

- Furthermore, reaction and solidification kinetics are required to make it even more realistic, since at the moment, a diffusion-limited system is assumed, while the growth rates may be affected by reaction kinetics at the interface.

7 ACKNOWLEDGEMENTS

I. Bellemans holds a research grant from the Research Foundation Flanders (12Z7720N). N. Vervliet holds a research grant from the Research Foundation Flanders (12ZM220N). This research received funding from the Flemish Government (AI Research Program). L. De Lathauwer and N. Vervliet are affiliated to Leuven.AI – KU Leuven institute for AI, B-3000, Leuven, Belgium. This work was supported by the Fonds de la Recherche Scientifique – FNRS and the Fonds Wetenschappelijk Onderzoek – Vlaanderen under EOS Project no 30468160 (SeLMA). L. De Lathauwer was further supported by KU Leuven Internal Funds: C16/15/059, IDN/19/014. Nele Moelans holds an ERC (European Research Council)-Starting Grant (INTERDIFFUSION, grant agreement no. 714754).

8 DATA AVAILABILITY

The raw data required to reproduce these findings are available to download as supplementary material with all code necessary to reproduce the factor matrices using Matlab and Tensorlab.

9 REFERENCES

[1] F. Vetere, H. Behrens, F. Holtz, G. Vilardo, G. Ventura, Viscosity of crystal-bearing melts and its implication for magma ascent, Journal of Mineralogical and Petrological Sciences. 105 (2010) 151–163. https://doi.org/10.2465/jmps.090402.

[2] D. Durinck, P.T. Jones, M. Guo, F. Verhaeghe, G. Heylen, R. Hendrickx, R. Baeten, B. Blanpain, P. Wollants, EAF stainless steel refining - Part II: Microstructural slag evolution and its implications for slag foaming and chromium recovery, Steel Research International. 78 (2007) 125–135. https://doi.org/10.1002/srin.200705869.

[3] I. Bellemans, E. De Wilde, N. Moelans, K. Verbeken, Metal losses in pyrometallurgical operations - A review, Advances in Colloid and Interface Science. 255 (2018) 47–63. https://doi.org/10.1016/j.cis.2017.08.001.

[4] Z. Liu, B. Blanpain, M. Guo, Viscosity of Partially Crystallized Bof Slag, in: 7th International Symposium on High-Temperature Metallurgical Processing, John Wiley & Sons, Inc., Hoboken, NJ, USA, 2016: pp. 263–269. https://doi.org/10.1002/9781119274643.ch33.

[5] O. Vergote, T. Suetens, I. Bellemans, K. Verbeken, Effect of solids and phase composition on rheology of secondary copper smelting slag, in: European Metallurgical Conference 2021, 2021.

[6] A. Fallah-Mehrjardi, P.C. Hayes, E. Jak, Understanding Slag Freeze Linings, Jom. 66 (2014) 1654–1663. https://doi.org/10.1007/s11837-014-1127-4.

[7] C.W. Bale, P. Chartrand, S.A. Degterov, G. Eriksson, K. Hack, R. Ben Mahfoud, J. Melançon, A.D. Pelton, S. Petersen, FactSage thermochemical software and databases, Calphad. 26 (2002) 189–228. https://doi.org/10.1016/S0364-5916(02)00035-4.
[8] N. Moelans, B. Blanpain, P. Wollants, An introduction to phase-field modeling of microstructure evolution, Calphad. 32 (2008) 268–294. https://doi.org/10.1016/j.calphad.2007.11.003.
[9] I. Bellemans, N. Moelans, K. Verbeken, Phase-Field Modelling in Extractive Metallurgy, Critical Reviews in Solid State and Materials Sciences. 43 (2018) 417–454. https://doi.org/10.1080/10408436.2017.1397500.
[10] R. Kobayashi, Modeling and numerical simulations of dendritic crystal growth, Physica D: Nonlinear Phenomena. 63 (1993) 410–423. https://doi.org/10.1016/0167-2789(93)90120-P.
[11] L.-Q. Chen, Phase-Field Models for Microstructure Evolution, Annual Review of Materials Research. 32 (2002) 113–140. https://doi.org/10.1146/annurev.matsci.32.112001.132041.
[12] A.A. Wheeler, W.J. Boettinger, G.B. McFadden, Phase-field model for isothermal phase transitions in binary alloys, Phys. Rev. A. 45 (1992) 7424–7439. https://doi.org/10.1103/PhysRevA.45.7424.
[13] J. Eiken, B. Böttger, I. Steinbach, Multiphase-field approach for multicomponent alloys with extrapolation scheme for numerical application, Phys. Rev. E. 73 (2006) 066122. https://doi.org/10.1103/PhysRevE.73.066122.
[14] R.S. Qin, H.K. Bhadeshia, Phase field method, Materials Science and Technology. 26 (2010) 803–811. https://doi.org/10.1179/174328409X453190.
[15] I. Steinbach, F. Pezzolla, B. Nestler, M. Seeßelberg, R. Prieler, G.J. Schmitz, J.L.L. Rezende, A phase field concept for multiphase systems, Physica D: Nonlinear Phenomena. 94 (1996) 135–147. https://doi.org/10.1016/0167-2789(95)00298-7.
[16] J. Tiaden, B. Nestler, H.J. Diepers, I. Steinbach, The multiphase-field model with an integrated concept for modelling solute diffusion, Physica D: Nonlinear Phenomena. 115 (1998) 73–86. https://doi.org/10.1016/S0167-2789(97)00226-1.
[17] S.G. Kim, W.T. Kim, T. Suzuki, Phase-field model for binary alloys, Phys. Rev. E. 60 (1999) 7186–7197. https://doi.org/10.1103/PhysRevE.60.7186.
[18] N. Moelans, A quantitative and thermodynamically consistent phase-field interpolation function for multi-phase systems, Acta Materialia. 59 (2011) 1077–1086. https://doi.org/10.1016/j.actamat.2010.10.038.
[19] J. Heulens, B. Blanpain, N. Moelans, A phase field model for isothermal crystallization of oxide melts, Acta Materialia. 59 (2011) 2156–2165. https://doi.org/10.1016/j.actamat.2010.12.016.
[20] S.Y. Hu, J. Murray, H. Weiland, Z.K. Liu, L.Q. Chen, Thermodynamic description and growth kinetics of stoichiometric precipitates in the phase-field approach, Calphad: Computer Coupling of Phase Diagrams and Thermochemistry. 31 (2007) 303–312. https://doi.org/10.1016/j.calphad.2006.08.005.
[21] N. Moelans, B. Blanpain, P. Wollants, Quantitative phase-field approach for simulating grain growth in anisotropic systems with arbitrary inclination and misorientation dependence, Physical Review Letters. 101 (2008) 025502. https://doi.org/10.1103/PhysRevLett.101.025502.

[22] M. Fleck, L. Mushongera, D. Pilipenko, K. Ankit, H. Emmerich, On phase-field modeling with a highly anisotropic interfacial energy, Eur. Phys. J. Plus. 126 (2011) 95. https://doi.org/10.1140/epjp/i2011-11095-7.
[23] O. Tschukin, A. Silberzahn, M. Selzer, P.G.K. Amos, D. Schneider, B. Nestler, Concepts of modeling surface energy anisotropy in phase-field approaches, Geothermal Energy. 5 (2017) 19. https://doi.org/10.1186/s40517-017-0077-9.
[24] N. Ma, Q. Chen, Y. Wang, Implementation of high interfacial energy anisotropy in phase field simulations, Scripta Materialia. 54 (2006) 1919–1924. https://doi.org/10.1016/j.scriptamat.2006.02.005.
[25] S. Torabi, J. Lowengrub, Simulating interfacial anisotropy in thin-film growth using an extended Cahn-Hilliard model, Phys. Rev. E. 85 (2012) 041603. https://doi.org/10.1103/PhysRevE.85.041603.
[26] J.J. Eggleston, G.B. McFadden, P.W. Voorhees, A phase-field model for highly anisotropic interfacial energy, Physica D: Nonlinear Phenomena. 150 (2001) 91–103. https://doi.org/10.1016/S0167-2789(00)00222-0.
[27] T. Uehara, R.F. Sekerka, Phase field simulations of faceted growth for strong anisotropy of kinetic coefficient, Journal of Crystal Growth. 254 (2003) 251–261. https://doi.org/10.1016/S0022-0248(03)01120-5.
[28] N. Vervliet, O. Debals, L. Sorber, L. De Lathauwer, Breaking the curse of dimensionality using decompositions of incomplete tensors: Tensor-based scientific computing in big data analysis, IEEE Signal Processing Magazine. 31 (2014) 71–79. https://doi.org/10.1109/MSP.2014.2329429.
[29] Y.A. Coutinho, N. Vervliet, L. De Lathauwer, N. Moelans, Combining thermodynamics with tensor completion techniques to enable multicomponent microstructure prediction, Npj Computational Materials. 6 (2020) 2. https://doi.org/10.1038/s41524-019-0268-y.
[30] J. Heulens, B. Blanpain, N. Moelans, Phase field modeling of the crystallization of FeOx–SiO2 melts in contact with an oxygen-containing atmosphere, Chemical Geology. 290 (2011) 156–162. https://doi.org/10.1016/j.chemgeo.2011.09.005.
[31] N. Moelans, B. Blanpain, P. Wollants, Quantitative analysis of grain boundary properties in a generalized phase field model for grain growth in anisotropic systems, Physical Review B - Condensed Matter and Materials Physics. 78 (2008) 024113. https://doi.org/10.1103/PhysRevB.78.024113.
[32] N. Moelans, Phase-field simulations of grain growth in materials containing second-phase particles, 2006. https://doi.org/10.1073/pnas.0703993104.
[33] J. Heulens, Isothermal crystallization of metallurgical slags, KU Leuven, 2011.
[34] S.G. Kim, W.T. Kim, T. Suzuki, Phase-field model for binary alloys, Physical Review E - Statistical Physics, Plasmas, Fluids, and Related Interdisciplinary Topics. 60 (1999) 7186–7197. https://doi.org/10.1103/PhysRevE.60.7186.
[35] L.Q. Chen, Phase-field models for microstructure evolution, Annual Review of Materials Science. 32 (2002) 113–140. https://doi.org/10.1146/annurev.matsci.32.112001.132041.
[36] J. Heulens, N. Moelans, On the rotation invariance of multi-order parameter models for grain growth, Scripta Materialia. 62 (2010) 827–830. https://doi.org/10.1016/j.scriptamat.2010.02.009.
[37] H. Larsson, L. Höglund, A scheme for more efficient usage of CALPHAD data in simulations, Calphad: Computer Coupling of Phase Diagrams and Thermochemistry. 50 (2015) 1–5. https://doi.org/10.1016/j.calphad.2015.04.007.

[38] A.D. Pelton, P. Chartrand, The modified quasi-chemical model: Part II. Multicomponent solutions, Metallurgical and Materials Transactions A: Physical Metallurgy and Materials Science. 32 (2001) 1355–1360. https://doi.org/10.1007/s11661-001-0226-3.
[39] P. Chartrand, A.D. Pelton, The modified quasi-chemical model: Part III. Two sublattices, Metallurgical and Materials Transactions A: Physical Metallurgy and Materials Science. 32 (2001) 1397–1407. https://doi.org/10.1007/s11661-001-0229-0.
[40] A.D. Pelton, P. Chartrand, G. Eriksson, The modified quasi-chemical model: Part IV. Two-sublattice quadruplet approximation, Metallurgical and Materials Transactions A: Physical Metallurgy and Materials Science. 32 (2001) 1409–1416. https://doi.org/10.1007/s11661-001-0230-7.
[41] J. Heulens, B. Blanpain, N. Moelans, Phase-field analysis of a ternary two-phase diffusion couple with multiple analytical solutions, Acta Materialia. 59 (2011) 3946–3954. https://doi.org/10.1016/j.actamat.2011.03.020.
[42] S. Petersen, K. Hack, The thermochemistry library ChemApp and its applications, Zeitschrift Fuer Metallkunde/Materials Research and Advanced Techniques. 98 (2007) 935–945. https://doi.org/10.3139/146.101551.
[43] ChemApp - The Thermochemistry Library for your Software, 2013.
[44] N.D. Sidiropoulos, L. De Lathauwer, X. Fu, K. Huang, E.E. Papalexakis, C. Faloutsos, Tensor Decomposition for Signal Processing and Machine Learning, IEEE Transactions on Signal Processing. 65 (2017) 3551–3582. https://doi.org/10.1109/TSP.2017.2690524.
[45] N. Vervliet, O. Debals, L. De Lathauwer, Canonical polyadic decomposition of incomplete tensors with linearly constrained factors, KU Leuven, ESAT-STADIUS Technical Report 16–17, Leuven, 2017.
[46] A. Borgenstam, A. Engström, L. Höglund, J. Ågren, DICTRA, a tool for simulation of diffusional transformations in alloys, Journal of Phase Equilibria. 21 (2000) 269–280. https://doi.org/10.1361/105497100770340057.
[47] Y. Ukyo, K.S. Goto, The interdiffusivity matrix of Fe2O3-CaO-SiO2 melt at 1693 to 1773 K, Metallurgical Transactions B. 12 (1981) 449–454. https://doi.org/10.1007/BF02654313.
[48] M.D. Dolan, R.F. Johnston, Multicomponent diffusion in molten slags, Metallurgical and Materials Transactions B: Process Metallurgy and Materials Processing Science. 35 (2004) 675–684. https://doi.org/10.1007/s11663-004-0008-6.
[49] M. Roskosz, C.M.O. Alexander, K. Sio, J. Wang, H.C. Watson, N. Dauphas, B.O. Mysen, Redox-dependent, diffusion-driven fractionation of Fe isotopes in silicate melts and its structural controls, in: 2010. https://www.goldschmidtabstracts.info/abstracts/abstractView?id=2010001683.
[50] J.-J. Liu, J. Heulens, M. Guo, N. Moelans, Isothermal Crystal Growth Behavior of CaSiO3 in Ternary Oxide Melts, Journal of Inorganic Materials. 31 (2016) 547–554. https://doi.org/10.15541/jim20150516.
[51] E. De Wilde, I. Bellemans, M. Campforts, A. Khaliq, K. Vanmeensel, D. Seveno, M. Guo, A. Rhamdhani, G. Brooks, B. Blanpain, N. Moelans, K. Verbeken, Wetting behaviour of Cu based alloys on spinel substrates in pyrometallurgical context, Materials Science and Technology (United Kingdom). 31 (2015) 1925–1933. https://doi.org/10.1179/1743284715Y.0000000052.
[52] E. De Wilde, I. Bellemans, M. Campforts, M. Guo, K. Vanmeensel, B. Blanpain, N. Moelans, K. Verbeken, Study of the Effect of Spinel Composition on Metallic Copper Losses in Slags, J. Sustain. Metall. 3 (2017) 416–427. https://doi.org/10.1007/s40831-016-0106-0.

[53] I. Bellemans, E. De Wilde, L. Claeys, T. De Seranno, M. Campforts, B. Blanpain, N. Moelans, K. Verbeken, Investigation of Reactive Origin for Attachment of Cu Droplets to Solid Particles, Metall and Materi Trans B. 48 (2017) 2459–2468. https://doi.org/10.1007/s11663-017-1051-4.
[54] D. Durinck, P.T. Jones, B. Blanpain, P. Wollants, Air-cooling of metallurgical slags containing multivalent oxides, Journal of the American Ceramic Society. 91 (2008) 3342–3348. https://doi.org/10.1111/j.1551-2916.2008.02597.x.
[55] R. Hill, P. Roeder, The Crystallization of Spinel from Basaltic Liquid as a Function of Oxygen Fugacity, The Journal of Geology. 82 (1974) 709–729. https://doi.org/10.1086/628026.
[56] N. Vervliet, O. Debals, L. Sorber, M. Van Barel, L. De Lathauwer, Tensorlab 3.0, Available online at www.tensorlab.net, 2016.
[57] W.A. Roos, J.H. Zietsman, Acceleration of complex equilibrium calculations for integration in high temperature models, in: Proceedings of MOLTEN 2020, 2020: pp. 28–30.
[58] V. Cnockaert, K. Maes, I. Bellemans, T. Crivits, H. Vrielinck, B. Blanpain, K. Verbeken, Quantification of the Fe3+ concentration in lead silicate glasses using X-band CW-EPR, Journal of Non-Crystalline Solids. 536 (2020) 120002. https://doi.org/10.1016/j.jnoncrysol.2020.120002.
[59] V. Cnockaert, I. Bellemans, T. Crivits, H. Vrielinck, B. Blanpain, K. Verbeken, Determination of the Fe3+/Sigma(Fe) Ratio in Synthetic Lead Silicate Slags Using X-Band CW-EPR, J. Sustain. Metall. (2021). https://doi.org/10.1007/s40831-021-00348-0.